Research Article

Growth Mechanisms and Morphology Engineering of Atomic Layer-Deposited WS$_2$

Hanjie Yang, Yang Wang, Xingli Zou, Rong-Xu Bai, Sheng Han, Zecheng Wu, Qi Han, Yu Zhang, Hao Zhu, Lin Chen, Xionggang Lu, Qingqing Sun,* Jack C. Lee, Edward T. Yu,* Deji Akinwande,* and Li Ji*
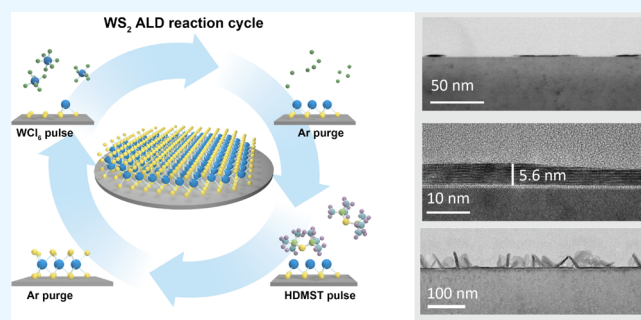
Read Online

ACCESS | Metrics & More | Article Recommendations | SI Supporting Information

ABSTRACT: Transition-metal dichalcogenides (TMDs) have attracted intense research interest for a broad range of device applications. Atomic layer deposition (ALD), a CMOS compatible technique, can enable the preparation of high-quality TMD films on 8 to 12 in. wafers for large-scale circuit integration. However, the ALD growth mechanisms are still not fully understood. In this work, we systematically investigated the growth mechanisms for WS$_2$ and found them to be strongly affected by nucleation density and film thickness. Transmission electron microscope imaging reveals the coexistence and competition of lateral and vertical growth mechanisms at different growth stages, and the critical thicknesses for each mechanism are obtained. The in-plane lateral growth mode dominates when the film thickness remains less than 5.6 nm (8 layers), while the vertical growth mode dominates when the thickness is greater than 20 nm. From the resulting understanding of these growth mechanisms, the conditions for film deposition were optimized and a maximum grain size of 108 nm was achieved. WS$_2$-based field-effect transistors were fabricated with electron mobility and on/off current ratio up to 3.21 cm^2 V^{-1} s^{-1} and 10^5, respectively. Particularly, this work proves the capability of synthesis of TMD films in a wafer scale with excellent controllability of thickness and morphology, enabling many potential applications other than transistors, such as nanowire- or nanosheet-based supercapacitors, batteries, sensors, and catalysis.

KEYWORDS: *transition-metal dichalcogenide, atomic layer deposition, wafer-scale, WS$_2$, field-effect transistors*

INTRODUCTION

Transition-metal dichalcogenides (TMDs), a family of layered materials with a composition of the form MX$_2$ (where M = transition metal such as W, Mo, Nb, Ti, etc., and X = S, Se, Te), are considered to be promising channel materials, particularly in the monolayer form, for alleviating short channel effects in field-effect transistors (FETs) as CMOS technology continues to scale down.[1,2] For example, monolayer WS$_2$ has a direct band gap of 1.9 eV instead of an indirect band gap of 1.4 eV for bulk WS$_2$,[3] enabling its promising applications in transistors,[4,5] integrated circuits,[6,7] photodetectors,[8] and valleytronic and spintronic devices.[9] For electronic and optoelectronic applications, layer numbers, defects, and grain boundaries have significant effects on the electrical and optical properties of TMDs.[10] Synthesis of TMDs can be achieved by both top-down and bottom-up methodologies. The top-down approach, represented by mechanical exfoliation, is ideal for research purposes that require ultra-high-quality monolayers[11−13] but is not well suited for the wafer-scale production. To address this issue, bottom-up methods, such as chemical vapor deposition (CVD), have been intensively studied.[14−16] Centimeter-scale

monolayer WS$_2$ thin films synthesized by CVD processes have been demonstrated[17−19] but precisely controlling thickness and uniformity across 8 or 12 in. wafers and depositing over 3D nanostructures with a very high aspect ratio remain very challenging.

Atomic layer deposition (ALD), a self-limiting reaction process that is widely used in the CMOS industry for high-k dielectric deposition and metallization, is considered to be a promising solution for preparing TMD films.[20−22] ALD, as a complementary technology with CVD, can be used to deposit TMD films with controllable thickness over high aspect ratio complex three-dimensional nanostructures.[23] However, several studies have indicated that the TMD growth mechanism in ALD does not obey the ideal self-limiting atomic-level growth
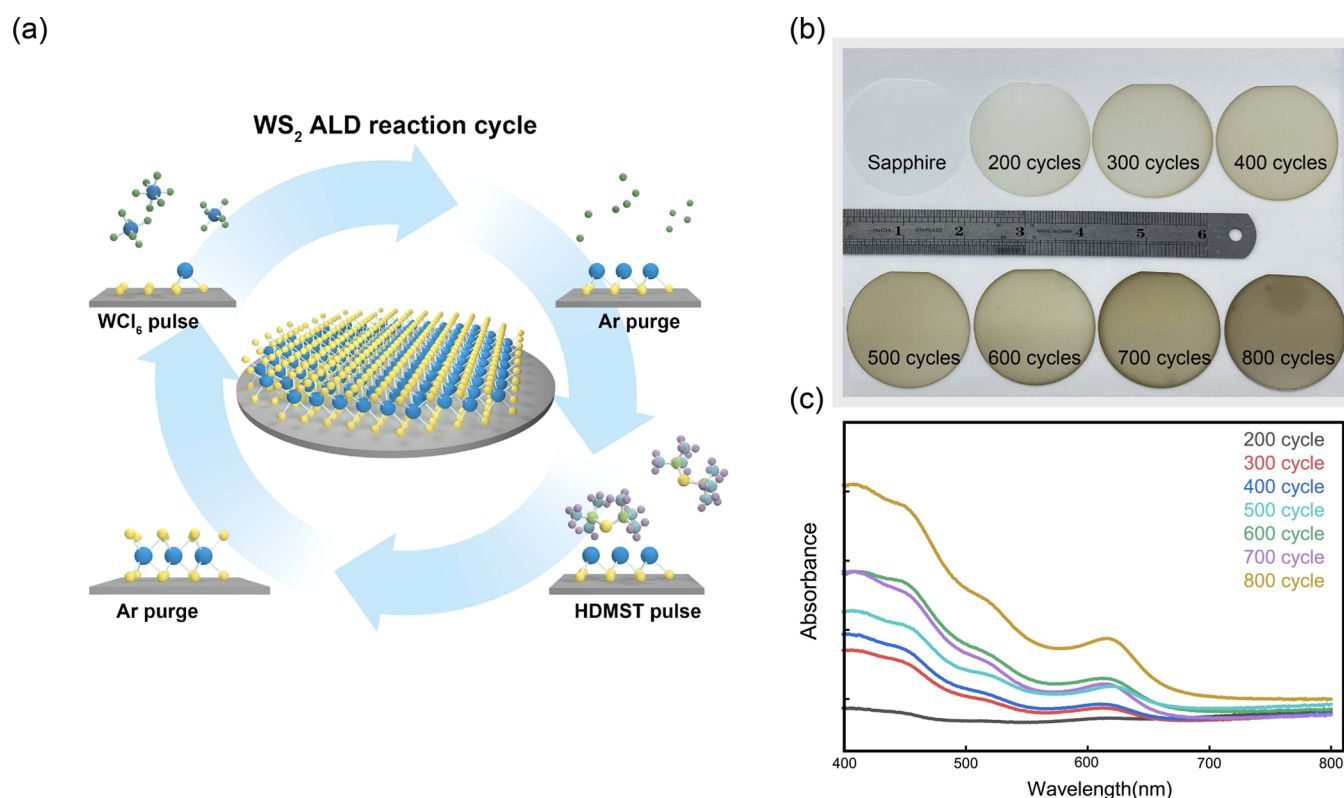
(a)

(b)

(c)

Figure 1. Illustration of ALD-grown WS$_2$ films on sapphire substrates. (a) Schematic of ALD-grown WS$_2$ films. (b) Photographs of sapphire substrate, 200, 300, 400, 500, 600, 700, and 800 ALD cycles growth on sapphires. (c) Ultraviolet−visible−near infrared (UV−vis−NIR) absorption spectra of WS$_2$ films with different thicknesses.

model, leading to unwanted morphologies.[24,25] For example, the ALD growth of atomically thin MoS$_2$ has been observed to exhibit a transition from lateral to vertical growth upon the coalescence of grains following initial nucleation upon the growth substrate.[25] These phenomena have been described in the literature, but a comprehensive study of ALD growth mechanisms is still lacking.

Herein, the growth mechanisms of ALD WS$_2$ were investigated in detail. By analyzing the morphologies and microstructures of as-grown films at different growth stages, it is found that the growth mechanisms governing the growth of WS$_2$ at different stages are controlled by the corresponding variations in nucleation densities. Specifically, the lateral growth mechanism during initial island growth results from low nucleation densities at the substrate surface; whereas a subsequently observed vertical growth mechanism is due to the increased nucleation densities on as-deposited films. With the help of this understanding, film growth was optimized for transistor applications. The average grain size was 50 nm and the maximum grain diameter reached 108 nm. Top-gated WS$_2$ FETs fabricated on the optimized films exhibit excellent electrical properties. The key achievement of this work is the successful clarification of the thickness-dependent growth mechanism and related device performance of ALD-grown WS$_2$ films, which should accelerate the realization of highly uniform TMD films to enable an excellent device performance to be achieved at a wafer scale. In addition, this understanding of growth mechanisms enables the realization of nanowire/ nanosheet morphologies, which are of interest for applications such as supercapacitors,[26] catalysts,[27] and sensors.[28]

RESULTS AND DISCUSSION

One typical cycle of the ALD synthesis process for WS$_2$ is illustrated in Figure 1a. Low-cost and less-toxic WCl$_6$ (99.9%) and (CH$_3$)$_3$SiSSi(CH$_3$)$_3$ (HMDST, 98%) precursors are successively introduced into the reaction chamber by a carrier gas (Ar). WS$_2$ films grow on sapphire substrates in a self-limiting reaction. The as-deposited WS$_2$ films are then post-annealed in a sulfur atmosphere at 950 °C for 2 h to fill the sulfur vacancies.

Figure 1b shows photographs of WS$_2$ samples with different ALD cycle numbers ranging from 300 to 800 cycles, confirming film uniformity over the entire 2 in. sapphire substrates for all samples. Because this work focuses principally on the investigation of growth mechanisms, we use 2 in. sapphire as standard substrates. As the number of cycles increases, the sample color becomes a deeper brown color. Figure 1c shows the absorption spectra of films with different thicknesses. The absorbance increases with an increasing number of ALD cycles, consistent with the steadily increasing film thickness. The A (617.1 nm, 2.01 eV) and B (514.3 nm, 2.41 eV) exciton peaks for WS$_2$ films grown with 300−800 ALD cycles can be clearly observed in the absorption curves. A and B exciton peaks were not found in WS$_2$ films with 200 cycles, indicating that the film did not result in fully formed films at this stage. The film thicknesses were measured by cross-sectional transmission electron microscopy (TEM) and atomic force microscopy (AFM). The cycle number-dependent thickness curve is plotted in Figure S1. AFM images at the five positions of the 600-cycle annealed WS$_2$ film are also shown in Figure S2, which confirmed the good uniformity of ALD-grown WS$_2$ films.
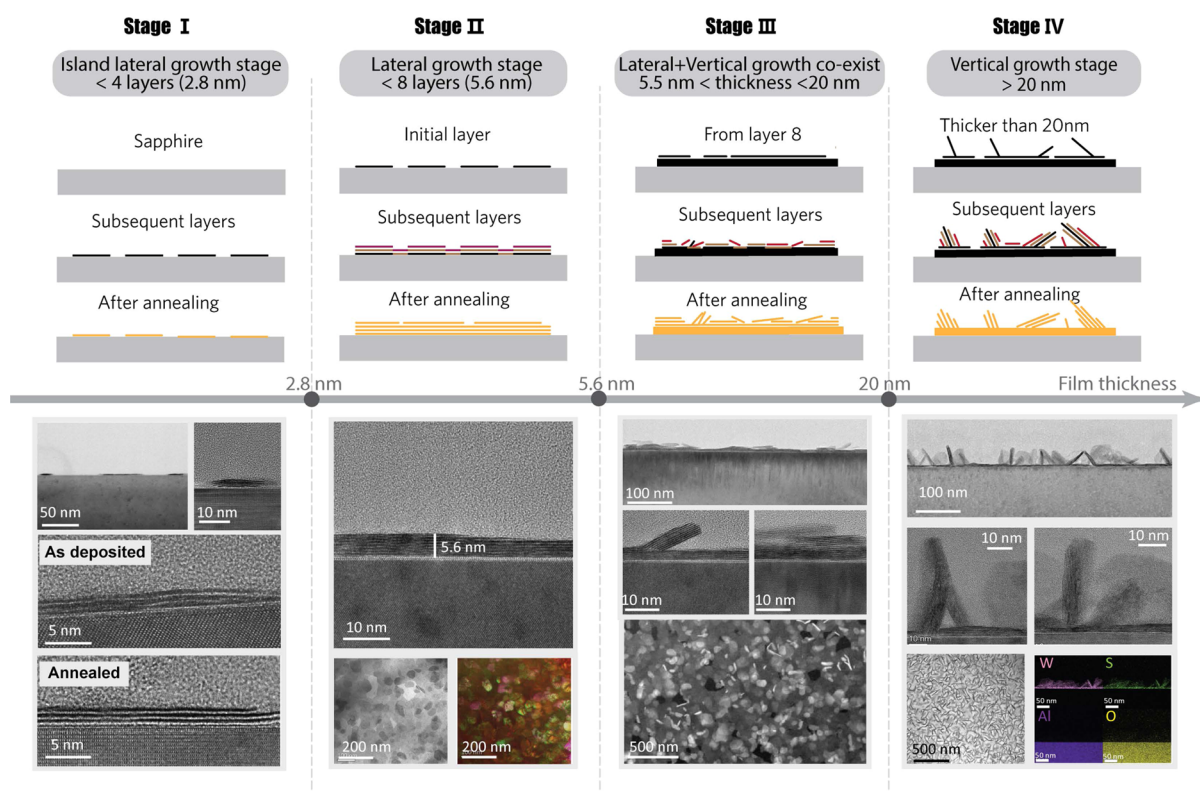
Figure 2. Growth mechanism of ALD WS_2 films. Schematic illustrations of different stages of growth are shown, along with corresponding TEM, and/or EDX spectroscopy images below each illustrated growth stage. The island growth stage (stage I) occurs first. Cross-sectional TEM images revealed island structures and non-connected films. TEM results without/with annealing are shown. The subsequent in-plane lateral growth mode (stage II) then dominates when the film remains thinner than eight layers, as revealed by top-view/cross-sectional TEM images of WS_2. Selected area electron diffraction patterns for films at the bottom right of stage II show the random orientation of different grains. Lateral and vertical growth modes coexist (stage III) when the thickness is in the range of 5.6−20 nm. TEM results reveal the initial appearance of wire microstructures during stage III. The vertical growth mode (stage IV) dominates when the thickness is greater than 20 nm, as illustrated in both the top-view and cross-sectional TEM. Fiber WS_2 and sapphire substrate elements are labeled with energy-dispersive X-ray (EDX) spectra.

To study the growth mechanisms of WS_2 films, the microstructure and morphology of the samples were characterized by scanning electron microscopy (SEM) and TEM imaging. The growth mechanism of ALD WS_2 involves both lateral and vertical growth processes, coexisting and competing with each other. SEM images of films at different growth stages are further described in the Supporting Information (Figure S3). As shown in Figure 2, at the initial stage (stage I), WS_2 first grew on sapphire in small islands or non-connected films, dominated by lateral growth. Island growth is frequently present in ALD processes for material growth.[29,30] As illustrated by TEM results for as-deposited samples and annealed samples, a layered structure consisting of the metal sandwiched in-between sulfur was clearly observed in annealed WS_2 films, indicating that the post-annealing treatment procedure is necessary for improving crystallinity, grain size, and horizontal alignment of basal planes. The islands continually expand and eventually form a smooth planar film, with a thickness of 8 layers up to 400 cycles, TEM images still show that the film is flat and continuous (Figure 2, stage II). No warpages or kinks were found in cross-sectional TEM images, confirming the preferred lateral growth orientation. The growth mode was affected by the nucleation densities and grain growth mechanism: when the nucleation density was very low, that is, thickness <8 layers, the lateral growth dominated. Due to the extremely low nucleation density on the substrate surface, after the formation of a WS_2 crystal nucleus, the

precursor can only adsorb at dangling bonds on the side of the WS_2 island leading to lateral growth, resulting in the rapid expansion of the WS_2 islands. However, due to the lack of a dangling bond on the top surface of the WS_2 islands, the films did not grow along the direction perpendicular to the substrate. As illustrated in Figure 2 (stage II), plan-view TEM results along with grain size analysis show an average grain size of 50 nm and a maximum grain diameter of 108 nm. EDX mapping of smooth planar film WS_2 films is shown in Figure S4, confirming the W and S elements of the WS_2 layers.

When the WS_2 films exceed 8 layers in thickness, lateral and vertical growths coexist. Warpages are observed on top of the films, and WS_2 grows along the warpages, which tended to form nanowires after annealing (Figure 2, stage III). Although previous literature reported that TMD materials prepared by ALD tend to appear in a nanowire morphology, the mechanism behind this tendency has not been explored.[24,25,31,32] The formation and growth of WS_2 crystal nuclei are very different from those formed during the island stage with low nucleation density. We believe that the appearance of defects led to the increase of nucleation density on the growth surface at this stage, and the presence of dislocations made the grains no longer grow along the lateral direction, resulting in the tiny warping morphology. The coexistence of planar films and nanowires confirms our proposed growth mechanism. As the thickness increased beyond 20 nm, vertical growth dominated. In this mode, as
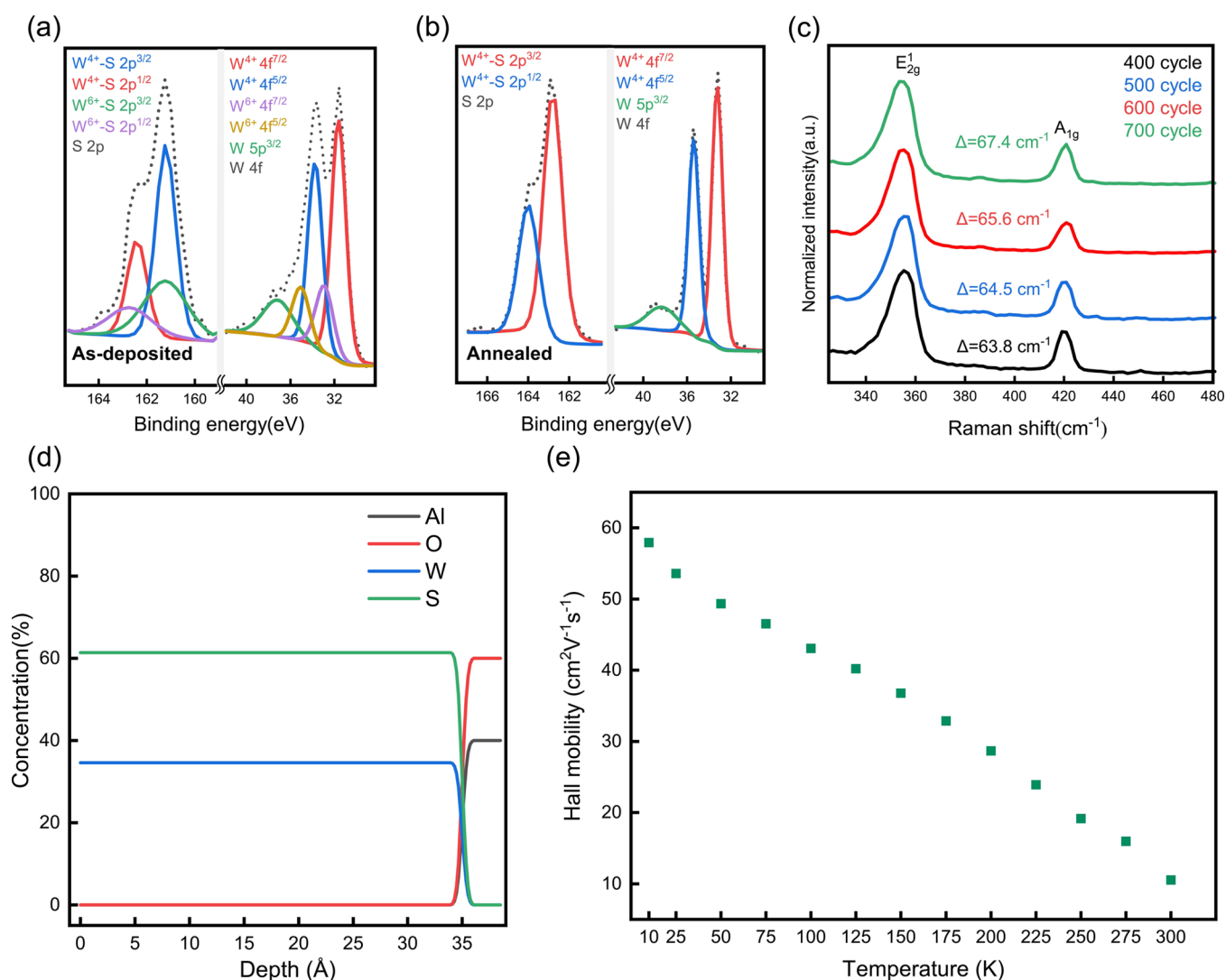
Figure 3. Materials characterization of ALD grown WS$_2$ films. (a) Fine XPS spectra of W 4f and S 2p peaks for as-deposited 400-cycle WS$_2$. Both WS$_2$ and WS$_{2+X}$ were observed. The W/S ratio was 1:2.3. (b) Fine XPS spectra of W 4f and S 2p of annealed 400-cycle WS$_2$. Only WS$_2$ was observed, indicating the necessity of annealing. The W/S ratio was 1:2.1. (c) Raman spectra of annealed WS$_2$ films with different film thicknesses. Δ shift increased when increasing the film thickness. (d) RBS of films with 3.5 nm thickness. (e) Electron Hall mobility of WS$_2$ at temperatures varying from 10 to 300 K.

the nucleation density keeps increasing, warpages and/or vertical nanowires tend to grow rapidly once the adjacent ones are contacted and merged together. Two vertically grown nanowires, as shown in Figure 2 (stage IV), are derived from warpages, and the interaction between the two microwarps leads to a transition in the direction of growth. The weakening of the van der Waals attraction as the number of layers increases may also be a possible contribution to this mechanism.[33,34] As a result, large amounts of perpendicular WS$_2$ nanowires could be observed, leading to a much faster vertical (perpendicular to the substrate surface) growth rate of nanowires compared to planar film growth (Figures S5 and S6). The non-linear growth rate after 700 cycles, as shown in Figure S1, also confirms this rule.

The stoichiometry and bonding states between W, S, and O atoms of 500-cycle smooth continuous WS$_2$ films before and after annealing were analyzed by XPS. Figure S7 shows the whole spectra of as-deposited and annealed WS$_2$ films. Core-level photoelectron spectra of W 4f and S 2p regions corroborated the importance of the annealing process to

improve the film quality, as shown in Figure 3a,b. Two doublets were fitted to the W 4f spectra in as-deposited samples, with WS$_2$ peaks at binding energies of 31.6 and 33.8 eV corresponding to the W^{4+}-S 4f$^{7/2}$ and W^{4+}-S 4f$^{5/2}$ levels, respectively; peaks corresponding to WS$_{2+X}$ are at 32.9 and 35.1 eV. In addition, two doublets were fitted to the S 2p spectra in the as-deposited samples; the peaks for W^{4+}-S 2p$^{3/2}$ and W^{4+}-S 2p$^{1/2}$ appear at 161.2 and 162.4 eV, while WS$_{2+X}$ corresponds to the binding energies of 161.3 and 162.8 eV. Before annealing, WS$_2$ films are in a sulfur-rich state, with a substantial presence of WS$_{2+X}$ components; the stoichiometric ratio of W/S was around 1:2.3. The coordination number of the W atom is higher in WS$_{2+X}$, the electrons in the orbital are attracted by the S atom more, resulting in the chemical displacement toward higher binding energy. After the film was annealed in a high-temperature sulfur atmosphere, it was found that the W 4f core-level photoelectron spectra changed significantly. Only a doublet corresponding to W 4f in WS$_2$ with binding energies of 33.2 eV (W^{4+}-S 4f$^{7/2}$) and 35.4 eV (W^{4+}-S 4f$^{5/2}$) was detected, and the peaks for W^{4+}-S 2p$^{3/2}$ and
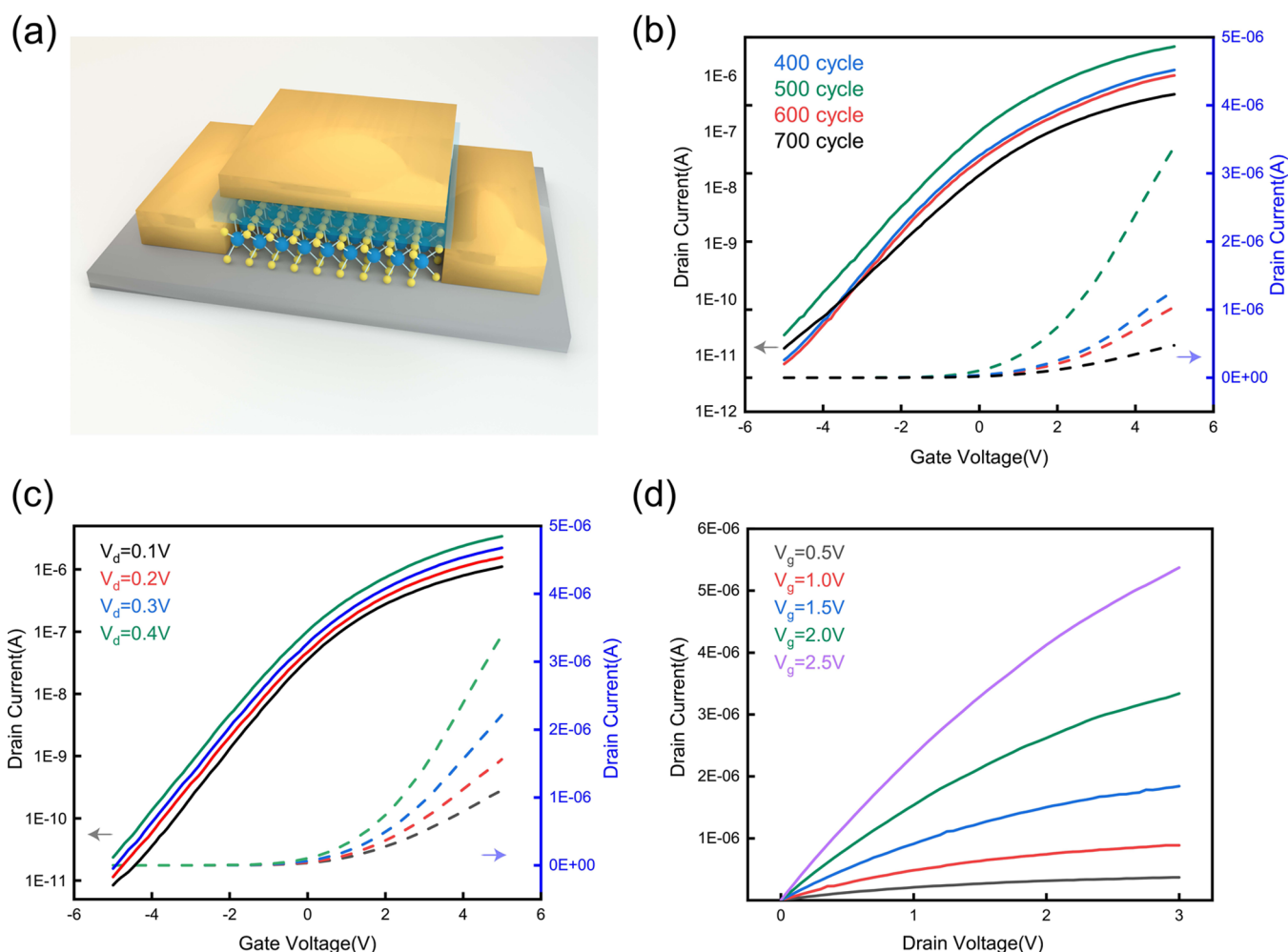
Figure 4. Transistor device geometry and characterization. (a) Schematic illustration of top-gated WS_2 FET on a sapphire substrate. (b) Transfer characteristics of WS_2 n-FET with 10 μm gate length and 40 μm gate width with different ALD cycles. (c) Transfer characteristics of 500 cycles WS_2 n-FET for drain voltages (V_d) of 0.1−0.4 V. The on-current reaches 3.4×10^{-6} A at a drain voltage of 0.4 V. (d) Output characteristics of 500 cycles WS_2 n-FET.

W^{4+}-S $2p^{1/2}$ appear at 162.8 and 163.9 eV. The peaks for W 4f and S 2p become sharper and the ratio between W and S is 1:2.1, which is very close to the standard stoichiometric value for WS_2.

The Raman spectra for WS_2 on sapphire with various thicknesses from 400 to 700 ALD cycles are shown in Figure 3c. The frequency difference "Δ shift" in the Raman spectra between the A_{1g} (plane vibration of S atoms) and E_{2g} (in-plane vibration of W and S atoms) modes has been used to determine the number of layers.[35] With increasing film thickness, the E_{2g} mode exhibited a clear red shift from 355.2 to 350.8 cm^{-1}, and the A_{1g} mode showed a slight blue shift from 419.1 to 420.9 cm^{-1}. The Δ shift increases from 63.8 to 67.4 cm^{-1} with the ALD cycle number from 400 to 700, which indicates that the WS_2 films become thicker. Such dependence of Raman shifts on film thickness further proves the thickness controllability in our ALD WS_2 synthesis method.

Rutherford backscattering spectrometry (RBS) measurements were performed under a backscattering angle of 160° and an appropriate grazing angle of 100° (with the sample oriented perpendicular to an incident He^{++} ion beam of 2.275 meV). The results show that the atomic concentrations of W and S are 34.6 and 61.4%, as shown in Figure 3d. The electron

Hall mobility of 400-cycle WS_2 was 57.94 $cm^2 V^{-1} s^{-1}$ at 10 K and 10.55 $cm^2 V^{-1} s^{-1}$ at 300 K, respectively, sufficient for transistor applications, as shown in Figure 3e. As shown in Figure S8, the X-ray diffraction (XRD) pattern of the smooth planar film with 400 ALD cycles shows intense peaks at 2θ values 14.08°, indexed to the (0002) planes of the 2H-WS_2 system, with the C axis perpendicular to the substrate as expected.

To evaluate the electrical properties of our ALD-grown WS_2 films, we fabricated top-gated FETs with 30 nm Al_2O_3 as the gate dielectric. The device architecture is shown in Figure 4a. WS_2 thin-film samples with different thicknesses were used from 300 to 700 ALD cycles. Ti/Au metallization was used to form metal contacts for source, drain, and gate. The transfer characteristic of WS_2 FETs with different thicknesses is shown in Figure 4b. The channel length and width are 10 and 40 μm, respectively, and the drain voltage is 0.4 V. The WS_2 FETs exhibited an n-type behavior with a large on/off current ratio up to 10^5. WS_2 FETs with a thickness of 300 ALD cycles were found not to work normally because the films prepared with fewer than 300 ALD cycles were not continuous and thus not suitable for device fabrication. From the transfer characteristic curves shown in Figure 4b, we confirm that the drain current I_d of the device increases with increasing thickness up to 500

Table 1. Benchmarks of ALD-Grown TMDs

reference	TMDs	wafer scale	growth method	I_{on}/I_{off}@4.6 mV/cm	controllable thickness	controllable morphology
this work	WS_2	8 in.	ALD	10^5	yes	yes
18, 19	WS_2	12 in.	ALD	N/A	yes	no
37	MoS_2	4 in.	ALD	N/A	yes	no
38	MoS_2	2 in.	ALD	N/A	yes	no
39	WSe_2	no	ALD	10^5	yes	no
40	MoS_2	no	ALD	N/A	N/A	no
22	MoS_2	no	ALD	N/A	yes	no

cycles. However, when cycle numbers exceed 600, the drain current decreases with increasing thickness. The field-effect mobility of the electrons was calculated from the transfer characteristic curve by using the equation: $\mu = (\Delta I_{ds}/\Delta V_{tg}) \times L/(WC_{ox}V_{ds})$, where L and W are the channel length and width, $C_{ox} = \varepsilon_1\varepsilon_0/d$ was the capacitance between the drain and the gate per unit area, ε_1, ε_0 are the dielectric constants of the Al_2O_3 layer and vacuum, and d is the thickness of the high-k dielectric. The electron mobility of WS_2 FETs with 500 ALD cycles is 3.21 cm^2 V^{-1} s^{-1}, while the values of 400, 600, and 700 ALD cycles are 1.49, 1.23, and 0.47 cm^2 V^{-1} s^{-1}, respectively. Due to the influence of contact resistance, the field-effect mobilities are generally much lower than the Hall mobility, which have been systematically investigated previously.[36] The fabricated FETs based on the 500-cycle WS_2 film presented the maximum drain current and the highest mobility. However, as the thickness increases, the vertical growth mode gradually dominates, the surface roughness increases rapidly and a large number of defects are generated, resulting in a drop of device performance. Although the degradation of device performance is within the acceptable range, the prospect that flat films can be used to produce superior device preparations is credible.

Figure 4c,d shows the transfer characteristic curve and output characteristic curve of the 500-cycle WS_2 FETs. The output characteristic indicates that the drain current nearly saturates at V_d = 3 V. This observation confirms the importance of the precise control of film thickness, that is, film surface morphology, for device performance. Table 1 shows the benchmarks of the ALD-prepared TMD films in recent years.

CONCLUSIONS

In summary, we have reported a systematic investigation of the WS_2 synthesis process using ALD. The results demonstrate that ALD-WS_2 synthesis can be precisely controlled in various morphologies. The nucleation mechanism and growth mechanism of WS_2 are greatly affected by the nucleation density. The abrupt increase of nucleation densities after continuous film formation leads to a change of the growth mechanism from lateral film growth to vertical nanowire growth. In different growth stages, lateral growth and vertical growth mechanisms coexist in competition with each other. Top-gated FETs based on the prepared WS_2 films show a high on/off ratio of 10^5 and field-effect carrier mobility of 3.21 cm^2 V^{-1} s^{-1}. In addition to WS_2 as studied in this work, growth and morphology control for other TMD materials would likely benefit from these insights. We believe this work sheds light on the synthesis of a wafer-scale continuous TMD film via ALD and provides a path for precisely controlling the layer numbers and sample morphologies for applications spanning from electronics and optoelectronics, requiring highly uniform thin-film morphologies, to sensing, catalytic and energy-related fields demanding nanostructured morphologies.

METHODS

Substrate. 2 in. c-plane single-crystal sapphires with a ⟨0001⟩ orientation and 0.5 mm thickness (Al_2O_3 > 99.99%) are used as the substrate. Before deposition, the substrates were successively cleaned in acetone and absolute alcohol with an ultrasonic bath for 15 min, respectively. The sample was then rinsed in deionized water to remove the residue from the previous step and dried by pure N_2 gas.

WS_2 Film Growth. The WS_2 films were deposited using a Beneq TFS-200 ALD reactor. Ar gas was purged into a reactor between the WCl_6 (99.9%) and $(CH_3)_3SiSSi(CH_3)_3$ (HMDST, 98%) pulse steps. The WCl_6 temperature was kept at 90 °C, while the HMDST was kept at room temperature. One cycle of ALD WS_2 deposition includes 1 s WCl_6 pulse time, followed by 12 s of purge time (99.99% Ar) and 1 s of HMDST pulse time, followed by 5 s of purge time, respectively. The reaction temperature in the reactor was set to 400 °C.

Annealing. After the ALD process, the as-deposited WS_2 film samples were placed in the central constant temperature area of the tube furnace at 950 °C, and 50 mg of the sulfur powder was placed and heated to form an appropriate sulfur atmosphere. The annealing time was 2 h and the ramping rate was 20 °C/min.

Characterization. X-ray photoelectron spectroscopy (XPS) was performed with an ULVAC PHI QuantERA II. A 1486 eV Al Kα anode was used as the source of X-ray radiation. Raman spectra were measured with a Nano LabRam HR Evolution Raman spectrometer using 532 nm laser excitation. The RBS instrument used for the analysis was a NEC Pelletron, model 3SDH. Hall effect measurements was performed with a Lakeshore 8400 instrument. X-ray diffraction were measured with a Bruker D8 ADVANCE. Absorption spectrum was obtained with an UV−vis−NIR spectrophotometer Agilent Cary 5000.

Device Fabrication. Annealed WS_2 films were first patterned by ultraviolet lithography to define the active area, with LOR 3A and S1813 as the adhesive and photoresist, respectively. CF_4 and Ar plasma were then used for etching in RIE (40/10 sccm, 150 W, 2 min). After the removal of the photoresistor with acetone, the source and drain were patterned by lithography and physical vapor deposition (15/70 nm Ti/Au), followed by a lift-off process. With trimethylaluminum and H_2O as precursors, 30 nm Al_2O_3 gate dielectric layer was grown at 250 °C using a Beneq TFS-200 ALD system. Finally, the Ti/Au top-gate electrodes were formed using the same process as for the source/drain electrodes.

Electrical Measurements. All of the electrical measurements were conducted using an Agilent B1500 semiconductor device analyzer under ambient conditions.

ASSOCIATED CONTENT

Ⓢ Supporting Information

The Supporting Information is available free of charge at https://pubs.acs.org/doi/10.1021/acsami.1c13467.

> Growth rate of the ALD WS_2 process; AFM images at five positions of the 600-cycle annealed WS_2 film; SEM images of films in different growth stages; EDX mapping of smooth planar film WS_2 films; HAADF-STEM and

BF-TEM images of perpendicular WS_2 nanowires; cross-sectional TEM of perpendicular WS_2 nanowires; full spectra of as-deposited and annealed WS_2 films; and XRD pattern of WS_2 films with 400 ALD cycles (PDF)

AUTHOR INFORMATION

Corresponding Authors

Qingqing Sun − *State Key Laboratory of ASIC and System, School of Microelectronics, Fudan University, Shanghai 200433, China;* orcid.org/0000-0002-6533-1834; Email: qqsun@fudan.edu.cn

Edward T. Yu − *Microelectronics Research Center, Department of Electrical and Computer Engineering, The University of Texas at Austin, Austin 78758 Texas, United States;* Email: ety@ece.utexas.edu

Deji Akinwande − *Microelectronics Research Center, Department of Electrical and Computer Engineering, The University of Texas at Austin, Austin 78758 Texas, United States;* orcid.org/0000-0001-7133-5586; Email: deji@ece.utexas.edu

Li Ji − *State Key Laboratory of ASIC and System, School of Microelectronics, Fudan University, Shanghai 200433, China;* orcid.org/0000-0002-2004-230X; Email: lji@fudan.edu.cn

Authors

Hanjie Yang − *State Key Laboratory of ASIC and System, School of Microelectronics, Fudan University, Shanghai 200433, China;* orcid.org/0000-0003-0544-6645

Yang Wang − *State Key Laboratory of ASIC and System, School of Microelectronics, Fudan University, Shanghai 200433, China*

Xingli Zou − *State Key Laboratory of Advanced Special Steel, School of Materials Science and Engineering, Shanghai University, Shanghai 200444, China*

Rong-Xu Bai − *State Key Laboratory of ASIC and System, School of Microelectronics, Fudan University, Shanghai 200433, China*

Sheng Han − *State Key Laboratory of ASIC and System, School of Microelectronics, Fudan University, Shanghai 200433, China*

Zecheng Wu − *State Key Laboratory of ASIC and System, School of Microelectronics, Fudan University, Shanghai 200433, China*

Qi Han − *State Key Laboratory of ASIC and System, School of Microelectronics, Fudan University, Shanghai 200433, China*

Yu Zhang − *State Key Laboratory of ASIC and System, School of Microelectronics, Fudan University, Shanghai 200433, China*

Hao Zhu − *State Key Laboratory of ASIC and System, School of Microelectronics, Fudan University, Shanghai 200433, China;* orcid.org/0000-0003-3890-6871

Lin Chen − *State Key Laboratory of ASIC and System, School of Microelectronics, Fudan University, Shanghai 200433, China;* orcid.org/0000-0002-7145-7564

Xionggang Lu − *State Key Laboratory of Advanced Special Steel, School of Materials Science and Engineering, Shanghai University, Shanghai 200444, China*

Jack C. Lee − *Microelectronics Research Center, Department of Electrical and Computer Engineering, The University of Texas at Austin, Austin 78758 Texas, United States*

Complete contact information is available at:

ACKNOWLEDGMENTS

REFERENCES

(1) Bhimanapati, G. R.; Lin, Z.; Meunier, V.; Jung, Y.; Cha, J.; Das, S.; Xiao, D.; Son, Y.; Strano, M. S.; Cooper, V. R.; Liang, L.; Louie, S. G.; Ringe, E.; Zhou, W.; Kim, S. S.; Naik, R. R.; Sumpter, B. G.; Terrones, H.; Xia, F.; Wang, Y.; Zhu, J.; Akinwande, D.; Alem, N.; Schuller, J. A.; Schaak, R. E.; Terrones, M.; Robinson, J. A. Recent Advances in Two-Dimensional Materials beyond Graphene. *ACS Nano* **2015**, *9*, 11509−11539.

(2) Li, J.; Yang, X.; Liu, Y.; Huang, B.; Wu, R.; Zhang, Z.; Zhao, B.; Ma, H.; Dang, W.; Wei, Z.; Wang, K.; Lin, Z.; Yan, X.; Sun, M.; Li, B.; Pan, X.; Luo, J.; Zhang, G.; Liu, Y.; Huang, Y.; Duan, X.; Duan, X. General synthesis of two-dimensional van der Waals heterostructure arrays. *Nature* **2020**, *579*, 368−374.

(3) Wang, Q. H.; Kalantar-Zadeh, K.; Kis, A.; Coleman, J. N.; Strano, M. S. Electronics and optoelectronics of two-dimensional transition metal dichalcogenides. *Nat. Nanotechnol.* **2012**, *7*, 699−712.

(4) Cheng, C.-C.; Chung, Y.-Y.; Li, U.-Y.; Lin, C.-T.; Li, C.-F.; Chen, J.-H.; Lai, T.-Y.; Li, K.-S.; Shieh, J.-M.; Su, S.-K.; Chiang, H.-L.; Chen, T.-C.; Li, L.-J.; Wong, H.-S. P.; Chien, C.-H. First demonstration of 40-nm channel length top-gate WS_2 pFET using channel area-selective CVD growth directly on SiO_x /Si substrate. *2019 Symposium on VLSI Technology*; IEEE, 2019; pp 244−245.

(5) Lee, J.; Chang, H.-Y.; Ha, T.-J.; Li, H.; Ruoff, R. S.; Dodabalapur, A.; Akinwande, D. High-performance flexible nanoelectronics: 2D atomic channel materials for low-power digital and high-frequency analog devices. *2013 IEEE International Electron Devices Meeting*; IEEE, 2013; pp 491−494.

(6) Huyghebaert, C.; Schram, T.; Smets, Q.; Kumar Agarwal, T.; Verreck, D.; Brems, S.; Phommahaxay, A.; Chiappe, D.; El Kazzi, S.; Lockhart de la Rosa, C.; Arutchelvan, G.; Cott, D.; Ludwig, J.; Gaur, A.; Sutar, S.; Leonhardt, A.; Marinov, D.; Lin, D.; Caymax, M.; Asselberghs, I.; Pourtois, G.; Radu, I. P. 2D materials: roadmap to CMOS integration. *2018 IEEE International Electron Devices Meeting (IEDM)*; IEEE, 2018; pp 512−515.

(7) Chiu, M. H.; Tang, H. L.; Tseng, C. C.; Han, Y.; Aljarb, A.; Huang, J. K.; Wan, Y.; Fu, J. H.; Zhang, X.; Chang, W. H.; Muller, D. A.; Takenobu, T.; Tung, V.; Li, L. J. Metal-Guided Selective Growth of 2D Materials: Demonstration of a Bottom-Up CMOS Inverter. *Adv. Mater.* **2019**, *31*, 1900861.

(8) Perea-López, N.; Elías, A. L.; Berkdemir, A.; Castro-Beltran, A.; Gutiérrez, H. R.; Feng, S.; Lv, R.; Hayashi, T.; López-Urías, F.; Ghosh, S.; Muchharla, B.; Talapatra, S.; Terrones, H.; Terrones, M. Photosensor Device Based on Few-Layered WS_2 Films. *Adv. Funct. Mater.* **2013**, *23*, 5511−5517.

(9) Jin, C.; Kim, J.; Utama, M. I. B.; Regan, E. C.; Kleemann, H.; Cai, H.; Shen, Y.; Shinner, M. J.; Sengupta, A.; Watanabe, K.; Taniguchi, T.; Tongay, S.; Zettl, A.; Wang, F. Imaging of pure spin-

valley diffusion current in WS$_2$-WSe$_2$ heterostructures. *Science* **2018**, *360*, 893.

(10) Hu, Z.; Wu, Z.; Han, C.; He, J.; Ni, Z.; Chen, W. Two-dimensional transition metal dichalcogenides: interface and defect engineering. *Chem. Soc. Rev.* **2018**, *47*, 3100−3128.

(11) Samadi, M.; Sarikhani, N.; Zirak, M.; Zhang, H.; Zhang, H. L.; Moshfegh, A. Z. Group 6 transition metal dichalcogenide nanomaterials: synthesis, applications and future perspectives. *Nanoscale Horiz.* **2018**, *3*, 90−204.

(12) Kshirsagar, C. U.; Xu, W.; Su, Y.; Robbins, M. C.; Kim, C. H.; Koester, S. J. Dynamic Memory Cells Using MoS$_2$ Field-Effect Transistors Demonstrating Femtoampere Leakage Currents. *ACS Nano* **2016**, *10*, 8457−8464.

(13) Chang, H.-Y.; Yang, S.; Lee, J.; Tao, L.; Hwang, W.-S.; Jena, D.; Lu, N.; Akinwande, D. High-Performance, Highly Bendable MoS$_2$ Transistors with High-K Dielectrics for Flexible Low-Power Systems. *ACS Nano* **2013**, *7*, 5446−5452.

(14) Han, S. A.; Bhatia, R.; Kim, S.-W. Synthesis, properties and potential applications of two-dimensional transition metal dichalcogenides. *Nano Convergence* **2015**, *2*, 17.

(15) Sarma, P. V.; Patil, P. D.; Barman, P. K.; Kini, R. N.; Shaijumon, M. M. Controllable growth of few-layer spiral WS$_2$. *RSC Adv.* **2016**, *6*, 376−382.

(16) Zhou, H.; Wang, C.; Shaw, J. C.; Cheng, R.; Chen, Y.; Huang, X.; Liu, Y.; Weiss, N. O.; Lin, Z.; Huang, Y.; Duan, X. Large Area Growth and Electrical Properties of p-Type WSe$_2$ Atomic Layers. *Nano Lett.* **2014**, *15*, 709−713.

(17) Yun, S. J.; Chae, S. H.; Kim, H.; Park, J. C.; Park, J.-H.; Han, G. H.; Lee, J. S.; Kim, S. M.; Oh, H. M.; Seok, J.; Jeong, M. S.; Kim, K. K.; Lee, Y. H. Synthesis of Centimeter-Scale Monolayer Tungsten Disulfide Film on Gold Foils. *ACS Nano* **2015**, *9*, 5510−5519.

(18) Kim, M.; Seo, J.; Kim, J.; Moon, J. S.; Lee, J.; Kim, J.-H.; Kang, J.; Park, H. High-Crystalline Monolayer Transition Metal Dichalcogenides Films for Wafer-Scale Electronics. *ACS Nano* **2021**, *15*, 3038−3046.

(19) Chubarov, M.; Choudhury, T. H.; Hickey, D. R.; Bachu, S.; Zhang, T.; Sebastian, A.; Bansal, A.; Zhu, H.; Trainor, N.; Das, S.; Terrones, M.; Alem, N.; Redwing, J. M. Wafer-Scale Epitaxial Growth of Unidirectional WS2 Monolayers on Sapphire. *ACS Nano* **2021**, *15*, 2532−2541.

(20) Schram, T.; Smets, Q.; Heyne, M. H.; Graven, B.; Kunnen, E.; Thiam, A.; Devriendt, K.; Delabie, A.; Lin, D.; Chiappe, D.; Asselberghs, I.; Lux, M.; Brus, S.; Huyghebaert, C.; Sayan, S.; Juncker, A.; Caymax, M.; Radu, I. P. BEOL compatible WS$_2$ transistors fully fabricated in a 300 mm pilot line. *2017 Silicon Nanoelectronics Workshop (SNW)*; IEEE, 2017; pp 139−140.

(21) Schram, T.; Smets, Q.; Groven, B.; Heyne, M. H.; Kunnen, E.; Thiam, A.; Devriendt, K.; Delabie, A.; Lin, D.; Lux, M.; Chiappe, D.; Asselberghs, I.; Brus, S.; Huyghebaert, C.; Sayan, S.; Juncker, A.; Caymax, M.; Radu, I. P. *WS$_2$ Transistors on 300 mm Wafers with BEOL Compatibility*; *2017 47th European Solid-State Device Research Conference (ESSDERC)*; IEEE, 2017; pp 212−215.

(22) Kim, H. Atomic layer deposition of metal and nitride thin films: Current research efforts and applications for semiconductor device processing. *J. Vac. Sci. Technol. B.* **2003**, *21*, 2231−2261.

(23) Mattinen, M.; Leskelä, M.; Ritala, M. Atomic Layer Deposition of 2D Metal Dichalcogenides for Electronics, Catalysis, Energy Storage, and Beyond. *Adv. Mater. Interfaces* **2021**, *8*, 2001677.

(24) Ho, T. A.; Bae, C.; Lee, S.; Kim, M.; Montero-Moreno, J. M.; Park, J. H.; Shin, H. Edge-On MoS$_2$ Thin Films by Atomic Layer Deposition for Understanding the Interplay between the Active Area and Hydrogen Evolution Reaction. *Chem. Mater.* **2017**, *29*, 7604−7614.

(25) Yang, J.; Liu, L. Trickle Flow Aided Atomic Layer Deposition (ALD) Strategy for Ultrathin Molybdenum Disulfide (MoS$_2$) Synthesis. *ACS Appl. Mater. Interfaces* **2019**, *11*, 36270−36277.

(26) Yun, Q.; Li, L.; Hu, Z.; Lu, Q.; Chen, B.; Zhang, H. Layered Transition Metal Dichalcogenide-Based Nanomaterials for Electrochemical Energy Storage. *Adv. Mater.* **2020**, *32*, 1903826.

(27) Tan, C.; Zhang, H. Two-dimensional transition metal dichalcogenide nanosheet-based composites. *Chem. Soc. Rev.* **2015**, *44*, 2713−2731.

(28) Gupta, A.; Sakthivel, T.; Seal, S. Recent development in 2D materials beyond graphene. *Prog. Mater. Sci.* **2015**, *73*, 44−126.

(29) Puurunen, R. L.; Vandervorst, W. Island growth as a growth mode in atomic layer deposition: A phenomenological model. *J. Appl. Phys.* **2004**, *96*, 7686−7695.

(30) Puurunen, R. L.; Vandervorst, W.; Besling, W. F. A.; Richard, O.; Bender, H.; Conard, T.; Zhao, C.; Delabie, A.; Caymax, M.; De Gendt, S.; Heyns, M.; Viitanen, M. M.; de Ridder, M.; Brongersma, H. H.; Tamminga, Y.; Dao, T.; de Win, T.; Verheijen, M.; Kaiser, M.; Tuominen, M. Island growth in the atomic layer deposition of zirconium oxide and aluminum oxide on hydrogen-terminated silicon: Growth mode modeling and transmission electron microscopy. *J. Appl. Phys.* **2004**, *96*, 4878−4889.

(31) Jiang, G.-Q.; Yao, C.-B.; Bao, S.-B.; Cai, Y. Standing growth mechanism and ultrafast nonlinear absorption properties of WS$_2$ films. *Opt. Mater.* **2020**, *106*, 109995.

(32) Sharma, A.; Verheijen, M. A.; Wu, L.; Karwal, S.; Vandalon, V.; Knoops, H. C. M.; Sundaram, R. S.; Hofmann, J. P.; Kessels, W. M. M.; Bol, A. A. Low-temperature plasma-enhanced atomic layer deposition of 2-D MoS$_2$: large area, thickness control and tuneable morphology. *Nanoscale* **2018**, *10*, 8615−8627.

(33) Ambrosetti, A.; Ferri, N.; Distasio, R. A.; Tkatchenko, A. Wavelike charge density fluctuations and van der waals interactions at the nanoscale. *Science* **2016**, *351*, 1171−1176.

(34) Ambrosetti, A.; Silvestrelli, P. L. Trends in graphene conductivity-change upon gas-adsorption: the relevance of orbital distortion. *J. Phys. Chem. Lett.* **2020**, *11*, 2737−2741.

(35) Berkdemir, A.; Gutiérrez, H.; Botello-Méndez, A.; Perea-López, N.; Elías, A.; Chia, C.; Wang, B.; Crespi, V.; López-Urías, F.; Charlier, J. Identification of individual and few layers of WS$_2$ using Raman Spectroscopy. *Sci. Rep.* **2013**, *3*, 1755.

(36) Nazir, G.; Khan, M. F.; Iermolenko, V. M.; Eom, J. Two- and four-probe field-effect and Hall mobilities in transition metal dichalcogenide fieldeffect transistors. *RSC Adv.* **2016**, *6*, 60787.

(37) Jang, Y.; Yeo, S.; Lee, H.-B. -R.; Kim, H.; Kim, S.-H. Wafer-scale, conformal and direct growth of MoS$_2$ thin films by atomic layer deposition. *Appl. Surf. Sci.* **2016**, *365*, 160−165.

(38) Tan, L. K.; Liu, B.; Teng, J. H.; Guo, S.; Low, H. Y.; Loh, K. P.; Chong, C. Y.; Yang, R. B.; Loh, K. P. Atomic layer deposition of a MoS$_2$ film. *Nanoscale* **2014**, *6*, 10584−10588.

(39) Browning, R.; Kuperman, N.; Solanki, R.; Kanzyuba, V.; Rouvimov, S. Large area growth of layered WSe$_2$ films. *Semicond. Sci. Technol.* **2016**, *31*, 095002.

(40) Jurca, T.; Moody, M. J.; Henning, A.; Emery, J. D.; Wang, B.; Tan, J. M.; Lohr, T. L.; Lauhon, L. J.; Marks, T. J. Low-Temperature Atomic Layer Deposition of MoS$_2$ Films. *Angew. Chem., Int. Ed. Engl.* **2017**, *56*, 4991−4995.